Dynamo action driven by precessional turbulence

Vivaswat Kumar [1,2,*], Federico Pizzi [1,3], George Mamatsashvili [1,4], André Giesecke [1],
Frank Stefani [1], and Adrian J. Barker [5]

[1]*Institute of Fluid Dynamics, Helmholtz-Zentrum Dresden-Rossendorf, Bautzner Landstraße 400, 01328 Dresden, Germany*
[2]*Institute of Process Engineering and Environmental Technology, Technische Universität Dresden, 01062 Dresden, Germany*
[3]*Department of Fluid Mechanics, Universitat Politécnica de Catalunya BarcelonaTech (UPC), Barcelona 08034, Spain*
[4]*E. Kharadze Georgian National Astrophysical Observatory, Abastumani 0301, Georgia*
[5]*Department of Applied Mathematics, School of Mathematics, University of Leeds, Leeds LS2 9JT, United Kingdom*

We reveal and analyze an efficient magnetic dynamo action due to precession-driven hydrodynamic turbulence in the local model of a precessional flow, focusing on the kinematic stage of this dynamo. The growth rate of the magnetic field monotonically increases with the Poincaré number Po, characterizing precession strength, and the magnetic Prandtl number Pm, equal to the ratio of viscosity to resistivity, for the considered ranges of these parameters. The critical Po_c for the dynamo onset decreases with increasing Pm. To understand the scale-by-scale evolution (growth) of the precession dynamo and its driving processes, we perform spectral analysis by calculating the spectra of magnetic energy and of different terms in the induction equation in Fourier space. To this end, we decompose the velocity field of precession-driven turbulence into two-dimensional (2D) vortical and three-dimensional (3D) inertial wave modes. It is shown that the dynamo operates across a broad range of scales and exhibits a remarkable transition from a primarily vortex-driven regime at lower Po to a more complex regime at higher Po where it is driven jointly by vortices, inertial waves, and the shear of the background precessional flow. Vortices and shear drive the dynamo mostly at large scales comparable to the flow system size, and at intermediate scales, while at smaller scales it is mainly driven by inertial waves. This study can be important not only for understanding the magnetic dynamo action in precession-driven flows, but also in a general context of flows where vortices emerge and govern the flow dynamics and evolution.

I. INTRODUCTION

Understanding the generation, amplification, and self-sustenance of magnetic fields in astrophysical and geophysical objects is the endeavor of dynamo theory [1–3]. From the magnetic field of our planet to distant stars and galaxies, magnetohydrodynamic (MHD) dynamo models offer insights into the complex interplay between flows of conducting fluids and fields, leading to the growth of the latter. To drive a dynamo, the kinetic energy of a flow must be transformed efficiently enough into magnetic energy, which in turn requires a strong driving mechanism for the flow.

Among the known driving mechanisms for planetary dynamos, precession-powered motion is a complementary candidate [4,5] to the more generally accepted driving by thermal convection [6]. Precession takes place when the rotation axis of a system periodically changes its orientation, producing a body force that drives a flow in the (liquid) interior of the precessing body [7]. In particular, precession-driven flows are potentially able to convert large amounts of kinetic energy (up to 10^{11}–10^{21} W [5,8,9]) to sustain the geomagnetic field [4]. This conversion can be due to instabilities [7,10] that give rise to vortices and may also trigger turbulence.

Precession-driven flows have been studied both experimentally [11–15] and theoretically via numerical simulations in global settings [16–25] to interpret those experiments. The capability of these flows to drive dynamos was demonstrated for laboratory flows in a specific parameter regime [15,19,21,26–30]. An alternative approach widely used in studies of precessional flows in astrophysical and geophysical contexts is a local model, which describes the dynamics of a small segment of celestial bodies (stars, gaseous planets, or the liquid cores of rocky planets) in a rotating Cartesian coordinate frame [31–34]. In this model, the laminar background flow induced by precession was shown to be subject to a precessional instability [35,36] and, consequently, this flow breaks down into a nonlinear (turbulent) state, composed of two basic modes—two-dimensional (2D) vortices and three-dimensional (3D) inertial waves [32–34]. As shown in these papers, the dynamical interplay among these two modes and the background shear flow determines the sustenance and energetic balances of the precessional turbulence.

In the present paper, following our previous hydrodynamical study of the precessional flow dynamics in the local model [34], we consider the MHD extension of this model and investigate a magnetic dynamo action enabled by this flow, focusing mainly on the kinematic stage of such dynamo. We demonstrate that this dynamo is powered by the precession-driven *turbulence* resulting from the nonlinear saturation of

---

*v.kumar@hzdr.de

065101-1

the precessional instability and characterize the dependence of its growth rate on the main control parameters of the flow, such as the Poincaré number Po, which characterizes precession strength, and the magnetic Prandtl number Pm, equal to the ratio of viscosity to resistivity. To understand the scale-by-scale dynamics of the magnetic field, we perform spectral analysis, studying the evolution of the magnetic energy spectrum and mechanisms of its amplification in Fourier space as a function of these two parameters. Our most important finding is that there is a remarkable transition from a dynamo driven by 2D vortices at smaller Po to one at higher Po driven jointly by 2D vortices, background precessional flow shear, and 3D inertial waves, which operate at different scales.

The paper is organized as follows: The physical model, the main equations, and the numerical setup are described in Sec. II. Analysis of the precession-driven dynamo in physical space is presented in Sec. III and in Fourier space in Sec. IV. Conclusions are given in Sec. V.

II. PHYSICAL MODEL AND MAIN EQUATIONS

In the local model, a precession-driven flow is considered in a Cartesian coordinate frame (x, y, z) rotating around the vertical z axis and precessing around another tilted x axis with angular velocities Ω and Po $\cdot \Omega$, respectively, where Po is the Poincaré number introduced above measuring precession strength. In this frame, precessional forcing gives rise to a laminar background flow with a linear shear along the z axis, which oscillates in time and is proportional to Po [31,32,34],

$$\boldsymbol{U}_0 = -2\Omega \cdot \text{Po} \cdot z[\sin(\Omega t), \cos(\Omega t), 0].$$

The velocity perturbation $\boldsymbol{u}$ about this precession-driven base flow and the magnetic field $\boldsymbol{B}$ are governed by the MHD equations for a conducting viscous and resistive incompressible fluid, which in the rotating and precessing frame take the form [32,34]

$$(\partial_t + \boldsymbol{U}_0 \cdot \nabla + \boldsymbol{u} \cdot \nabla)\boldsymbol{u}$$
$$= -\frac{1}{\rho}\nabla\Pi + \frac{1}{\mu_0\rho}(\boldsymbol{B} \cdot \nabla)\boldsymbol{B} + \nu\nabla^2\boldsymbol{u}$$
$$- 2\Omega\boldsymbol{e}_z \times \boldsymbol{u} - 2\Omega\boldsymbol{\varepsilon}(t) \times \boldsymbol{u} + 2\Omega u_z\boldsymbol{e}_z \times \boldsymbol{\varepsilon}(t), \quad (1)$$

$$(\partial_t + \boldsymbol{U}_0 \cdot \nabla)\boldsymbol{B} = \nabla \times (\boldsymbol{u} \times \boldsymbol{B}) + \eta\nabla^2\boldsymbol{B} - 2\Omega B_z\boldsymbol{e}_z \times \boldsymbol{\varepsilon}(t),$$
$$(2)$$

$$\nabla \cdot \boldsymbol{u} = \nabla \cdot \boldsymbol{B} = 0, \quad (3)$$

where ρ is the constant density of the fluid, Π is the sum of thermal and magnetic pressures, ν is the constant kinematic viscosity, μ_0 is the permeability of vacuum, and η is the constant magnetic diffusivity. The vector $\boldsymbol{\varepsilon}(t) = \text{Po}[\cos(\Omega t), -\sin(\Omega t), 0]$ describes the effects of precession in these equations: Coriolis acceleration due to precession, $-2\Omega\boldsymbol{\varepsilon}(t) \times \boldsymbol{u}$, and the stretching term $2\Omega u_z\boldsymbol{e}_z \times \boldsymbol{\varepsilon}(t)$ of the perturbation velocity due to the shear of the background flow $\boldsymbol{U}_0$ in Eq. (1), which jointly give rise to the precessional instability [35–37]. A similar stretching term $-2\Omega B_z\boldsymbol{e}_z \times \boldsymbol{\varepsilon}(t)$ related to the shear in Eq. (2) describes the growth of the magnetic field at the expense of free energy of the background flow.

The flow is considered in a periodic cubic box with the same length L in all directions, $L_x = L_y = L_z = L$. This box represents a small portion of a global precessional flow far from the actual boundaries of a system. In this case, we adopt the mixed shear-periodic boundary conditions briefly summarized below, which are commonly used in the local model of the flow [32–34]. We cannot directly apply standard periodic boundary conditions because the advection term $\boldsymbol{U}_0 \cdot \nabla$ on the left-hand side of Eqs. (1) and (2) depends linearly on z due to the flow shear. To circumvent this, we transform (x, y, z) coordinates to the frame (x', y', z') co-moving with the streamlines of the background flow $\boldsymbol{U}_0$,

$$x' = x - 2\text{Po}\cos(\Omega t)z, \quad (4)$$

$$y' = y + 2\text{Po}\sin(\Omega t)z, \quad (5)$$

$$z' = z. \quad (6)$$

In this co-moving frame, the advection term is absent and we can impose the usual periodic boundary conditions in the (x', y', z') coordinates with the period lengths L_x, L_y, and L_z, respectively. After transforming back to the original frame (x, y, z), these boundary conditions take the periodic form in x and y,

$$f(x, y, z, t) = f(x + L_x, y, z, t) \quad (x \text{ boundary}), \quad (7)$$

$$f(x, y, z, t) = f(x, y + L_y, z, t) \quad (y \text{ boundary}), \quad (8)$$

but shear-periodic form in z,

$$f(x, y, z, t) = f[x + 2\text{Po} \cdot \cos(\Omega t)L_z, y - 2\text{Po}\cdot$$
$$\times \sin(\Omega t)L_z, z + L_z, t] \quad (z \text{ boundary}), \quad (9)$$

where $f \in \{\boldsymbol{u}, \Pi, \boldsymbol{B}\}$. These shear-periodic boundary conditions resemble those used in the widely known shearing box model of accretion disks [38]. We note that the use of this local model with the associated shear-periodic boundary conditions is expected to be valid for modes with length scales smaller than the box size, but it becomes less suitable to describe larger structures comparable to the box size. Nevertheless, being devoid of real (rigid) boundary effects, this model is well suited for understanding the basic influence of precession on the dynamo action.

We normalize time by Ω^{-1}, lengths by L, velocities by ΩL, magnetic fields by $\Omega L(\mu_0\rho)^{1/2}$, and pressure by $\rho L^2\Omega^2$. With these normalizations, the kinetic and magnetic energy densities take the form $E_v = \boldsymbol{u}^2/2$ and $E_m = \boldsymbol{B}^2/2$, respectively. Besides the Poincaré number, the main parameters of the flow are the Reynolds number $\text{Re} = \Omega L^2/\nu$ and magnetic Prandtl number $\text{Pm} = \nu/\eta$. In real astrophysical and geophysical objects, precession is usually weak and hence the Poincaré number is small, $\text{Po} \ll 1$, while the Reynolds number is quite high [32]. In a first attempt to approach such a regime, we fix $\text{Re} = 3 \times 10^4$ and explore a broad range of $\text{Po} = 0.075$–0.4 and $\text{Pm} = 0.1$–10, while the dependence on Re will be analyzed elsewhere.

We solve Eqs. (1)–(3) supplemented with the shear-periodic boundary conditions (7)–(9) using the spectral code SNOOPY [39] adapted to the considered model of a precessional flow in Ref. [32]. Resolution for $\text{Pm} < 1$, i.e., when
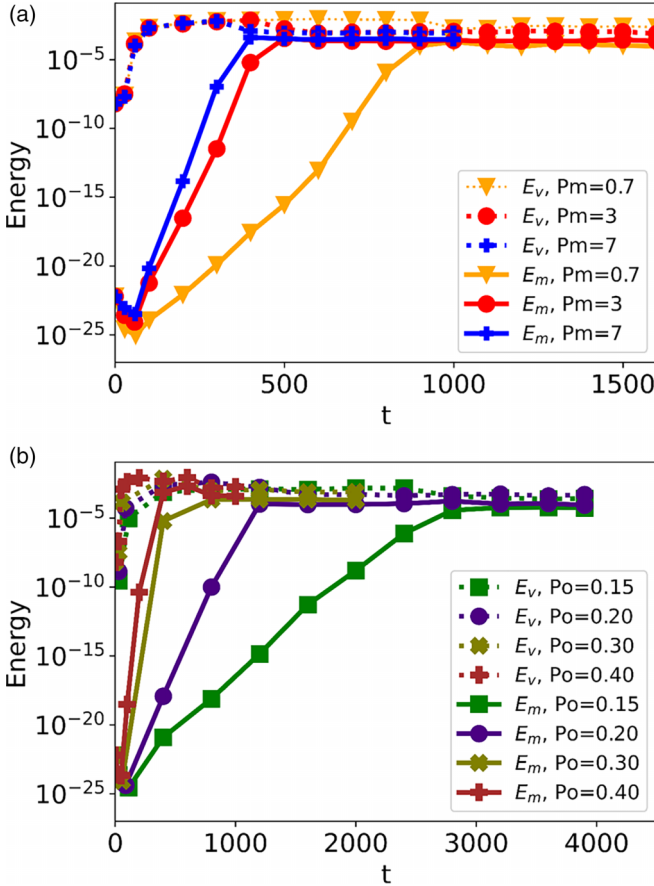
FIG. 1. Evolution of the volume-averaged kinetic $\langle E_v \rangle$ (dotted) and magnetic $\langle E_m \rangle$ (solid) energies at Re $= 3 \times 10^4$ for (a) different Pm at Po = 0.3 and (b) different Po at Pm = 3. The magnetic field energy starts to grow after the saturation of the precessional instability and increases exponentially by several orders of magnitude, indicating an efficient dynamo action due to precession-driven turbulence.

the viscous scale is shortest, is set as in [34]: $(N_x, N_y, N_z) = (128, 128, 128)$ at Po $\leqslant 0.125$ and $(256, 256, 256)$ at Po > 0.125. On the other hand, for Pm > 1, i.e., when resistive scale λ_η is shortest instead, resolution is increased by a factor of Pm$^{1/2}$. This is because the corresponding resistive wave number $k_\eta = 2\pi/\lambda_\eta$ to be resolved in the code scales as $k_\eta \sim$ Pm$^{1/2}$ at Pm > 1 [3] and therefore resolution is adjusted accordingly. Solenoidal random velocity perturbations with rms 1.12×10^{-4} and a very small random (seed) magnetic field with rms 10^{-12} are initially imposed, so that the back reaction of the magnetic field on the flow remains negligible during the early growth phases of the field. This allows us to analyze the dynamics of the dynamo in the kinematic stage, which we mainly focus on in this paper.

III. DYNAMO DUE TO PRECESSION-DRIVEN TURBULENCE

Figure 1 shows the evolution of the volume-averaged kinetic $\langle E_v \rangle$ and magnetic $\langle E_m \rangle$ energies at different Po and Pm, which indicates a two-stage dynamo process at work. In the beginning, the kinetic energy grows exponentially
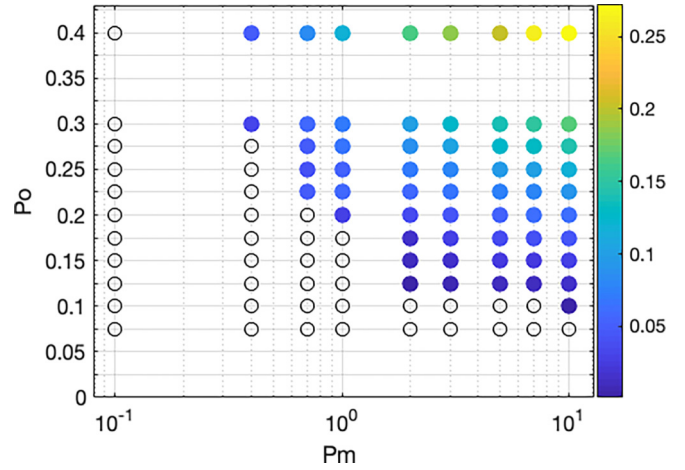

FIG. 2. Dynamo growth rate γ in the (Pm, Po) plane at Re $= 3 \times 10^4$ indicated by colored points, whereas there is no dynamo at the empty points. The colored and empty points together represent all the simulation runs done in this work.

as a result of the linear precessional instability, while the magnetic energy decreases. After several precession times $\sim (\epsilon \Omega)^{-1}$, the exponential growth saturates due to nonlinearity [advection term $(\boldsymbol{u} \cdot \boldsymbol{\nabla})\boldsymbol{u}$ in Eq. (1)] and, as a result, the flow settles down into a quasisteady turbulence composed of 2D vortices and 3D inertial waves ([32,34]; see Sec. IV below). Note that the dynamo action—exponential growth of the magnetic field—starts only *after* saturation of the precession instability and is driven by the nonlinear (turbulent) velocity perturbations. After several hundred rotation periods, the magnetic field growth saturates nonlinearly due to the back reaction of the Lorentz force on the flow, which is discernible by the small drop in $\langle E_v \rangle$ at the saturation point of $\langle E_m \rangle$ (Fig. 1). The growth rate of the magnetic energy, $\gamma = d \ln \langle E_m \rangle / dt$, in the kinematic regime and its nonlinear saturation level increase, and hence the dynamo is more efficient, with increasing Po and/or Pm. This dependence on Po and Pm is further explored in Fig. 2, which shows γ in the (Po, Pm) plane and summarizes all of the simulation runs done. Note, also, in this diagram that the critical Po$_c$ for the dynamo onset decreases with increasing Pm.

Figure 3 shows the structures of the vertical vorticity $\omega_z = (\boldsymbol{\nabla} \times \boldsymbol{u})_z$ in physical space at Po = 0.15 and, at the same instants, the induced vertical field B_z during the kinematic stage in two runs at Pm = 3 and 7. We observe vertically nearly uniform larger-scale columnar vortices embedded in a sea of smaller-scale 3D inertial waves, as is typical of precession-driven turbulence [32–34]. The traces of these vortices are visible in the magnetic field since vortices are, in fact, the main drivers of the dynamo at this small Po, as it will be shown in Sec. IV B (see Fig. 5). Note that although the magnetic field is induced mainly by these large-scale vortices, the characteristic length scale of the field structures is still smaller than that of the vortices and decreases with increasing Pm. This behavior is also observed in the spectral analysis in the next section.

IV. SPECTRAL ANALYSIS

To analyze dynamo action across length scales, we decompose the magnetic field into spatial Fourier modes both in the
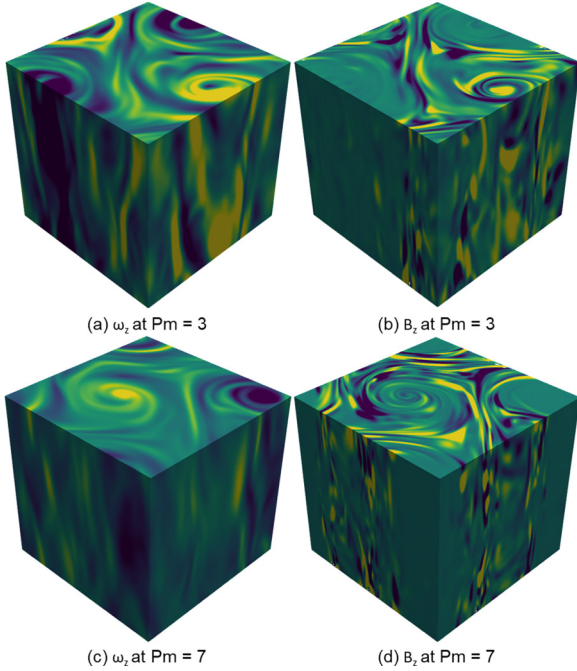
(a) ω_z at Pm = 3   (b) B_z at Pm = 3

(c) ω_z at Pm = 7   (d) B_z at Pm = 7

FIG. 3. Spatial distributions of the vertical vorticity $\omega_z = (\nabla \times \boldsymbol{u})_z$ at Po = 0.15 in two runs at (a) Pm = 3 and (c) Pm = 7, alongside the corresponding induced vertical field B_z in (b) and (d), respectively. For each Pm, the snapshots of ω_z and B_z are shown at equal instants during the kinematic regime. The characteristic length scale of the magnetic field structures is smaller than that of vortices and further decreases with increasing Pm.

co-moving (x', y', z') and original (x, y, z) reference frames [32,34],

$$\boldsymbol{B} = \sum_{\boldsymbol{k}} \bar{\boldsymbol{B}} \exp(ik_x x' + ik_y y' + ik_{z0} z')$$

$$= \sum_{\boldsymbol{k}} \bar{\boldsymbol{B}} \exp[ik_x x + ik_y y + ik_z(t)z]. \qquad (10)$$

In the co-moving frame, the variables are all periodic and hence this decomposition has a standard form with the constant wave numbers k_x, k_y, and k_{z0}, whereas in the (x, y, z) coordinates, the vertical wave number k_z varies with time. Indeed, using the invariance of the mode phases under the co-ordinate transformation, we can determine the wave numbers in the original frame by substituting transformation (4)–(6) in Fourier decomposition (10), regrouping the terms, and equating the coefficients of x, y, and z in the phases of both exponents. As a result, we find that the horizontal wave numbers k_x and k_y, which do not depend on time, are the same in both frames, whereas the vertical wave number $k_z(t)$ oscillates in time about an average value k_{z0},

$$k_z(t) = k_{z0} + 2\text{Po}[-k_x\cos(t) + k_y\sin(t)], \qquad (11)$$

thereby ensuring that the spatial Fourier modes satisfy the shearing-periodic boundary conditions (7)–(9) in the (x, y, z) frame ($\Omega = 1$ in our units). Physically, the time variation of k_z is, brought about by the background shear flow $\boldsymbol{U}_0$, which advects the spatial Fourier modes (via the term $\boldsymbol{U}_0 \cdot \nabla$),

causing the wave-vector component along the direction (z) of the flow shear to change periodically in time.

As is commonly done in turbulence and dynamo theory, below we will use the spherical shell average of any spectral quantity $\bar{f}(\boldsymbol{k})$ (energy spectra, dynamical terms, etc.) in Fourier space, which at a time t is defined in a standard way as $\sum_{k \leqslant |\boldsymbol{k}| \leqslant k+\Delta k} \bar{f}(\boldsymbol{k})$, with the summation assumed over Fourier modes inside spherical shells with a given wave-number magnitude (radius) $|\boldsymbol{k}| = k = (k_x^2 + k_y^2 + k_z^2)^{1/2}$ and width Δk [40]. Here, $k_i = n_i \Delta k$, $i \in \{x, y, z\}$, are the discrete wave numbers in the cubic box with integer $n_i = 0, \pm1, \pm2, \ldots, \pm(N_i/2 - 1)$ and $\Delta k = 2\pi/L$ is the grid cell size in Fourier space, i.e., the minimum nonzero wave number in this box.

Figure 4 shows the shell-averaged magnetic energy spectrum $\mathcal{E}_m(k) = |\bar{\boldsymbol{B}}|^2/2$ in the middle and at the end of the kinematic stage, together with the corresponding growth rate $\gamma(k)$ versus k at different Po and Pm. Note that in all the cases, the growth rate is nearly constant and positive, $\gamma(k) > 0$, at lower and intermediate $k \lesssim 100$, indicating the dynamo to be at work at these wave numbers, and decreases, turning negative, at higher k due to resistive dissipation (see Fig. 5). At small Po = 0.15, the growth rate weakly increases with Pm, mostly at higher wave numbers [Fig. 4(a)]. As a result, the energy spectra at Pm = 3 and 7 have nearly the same shape and magnitude at small and intermediate wave numbers, both during and at the end of the growth phase, while at high wave numbers, they are steeper at Pm = 3 than at Pm = 7. The magnetic energy spectrum and $\gamma(k)$ depend more strongly on Pm at higher Po = 0.3 and 0.4, as seen in Figs. 4(b) and 4(c), respectively. For a given Po and increasing Pm, the positive growth rate also increases and extends to higher k because of decreasing resistive dissipation (at a given Re). So, the spectra grow faster and are shallower at high k for higher Pm.

Comparing now the behavior of the magnetic energy spectra for different Po and a given Pm in Fig. 4, we notice that with increasing Po, $\gamma(k)$ moderately increases, although the maximum k_m up to which there is still a dynamo does not appear to change much from Pm = 0.7 to 3. This critical wave number increases with Po at higher Pm = 7 because of stronger driving by waves at high k (see below), so the magnetic spectra are shallower at high k for Po = 0.3 and 0.4 than those for Po = 0.15.

To summarize, in all the cases, the magnetic energy spectrum spans a broad range of scales, from the smallest wave numbers corresponding to the system size up to the highest ones of resistive dissipation. Hence, the precession dynamo appears to be neither only of large-scale nor only of small-scale type. The spectrum reaches a maximum at intermediate wave numbers, $10 \lesssim k \lesssim 100$, with a specific value in each case depending on Po and Pm and being lower for lower values of these two parameters. Below we examine which modes of motion in the precession-driven turbulence are mainly responsible for the dynamo growth at different k's.

A. Decomposition into vortical and wave modes

The precession-driven hydrodynamic turbulence represents a special case of forced rotating turbulence, where
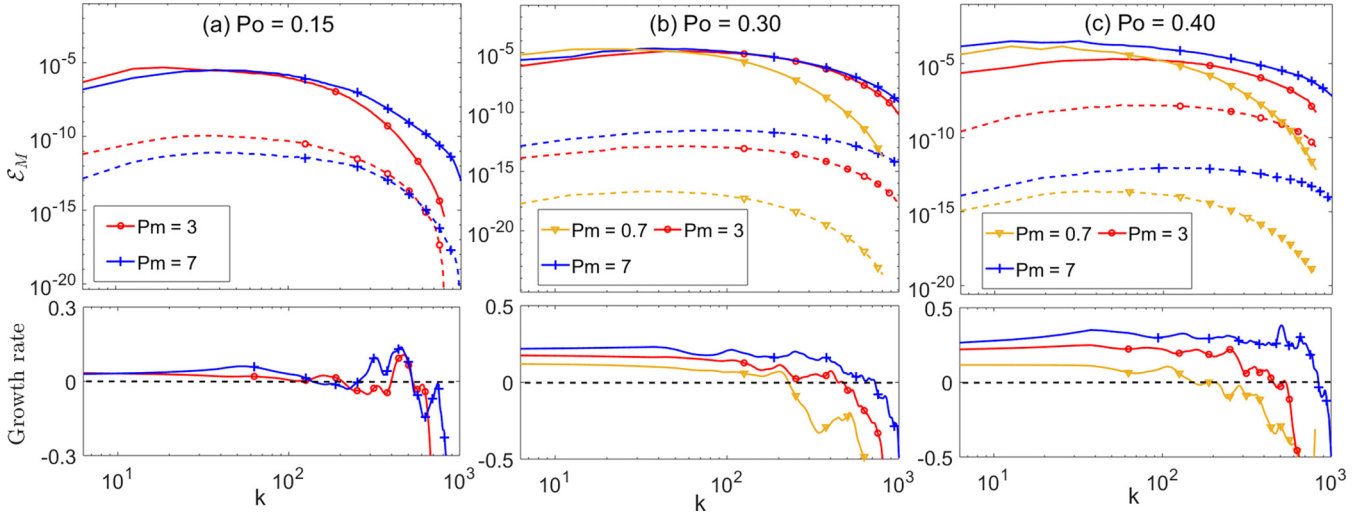
FIG. 4. Top row: Shell-averaged magnetic energy spectra in the middle (dashed) and at the end (solid) of the kinematic stage of the dynamo at various Pm for (a) Po = 0.15, (b) 0.3, and (c) 0.4. Bottom row: The corresponding growth rate $\gamma(k)$ of the spectral magnetic energy vs k. There is no dynamo at Po = 0.15 and Pm = 0.7, hence the yellow curve is absent in (a).

precession acts as a forcing agent over a broad range of wave numbers. Rotating turbulence has been very extensively studied in the literature (see a review [40] and references therein). One of the main tools of analysis is the decomposition of a turbulent flow field into two basic types of perturbation modes—vortices and inertial waves [40–42], which play key roles in the turbulence dynamics and energetic balances. An analogy between forced rotating turbulence and precession-driven turbulence has motivated the application of the similar mode decomposition method to the latter [32–34]. In the kinematic regime, Lorentz forces are negligible, so following those studies we can classify these two basic modes as done in the hydrodynamic case:
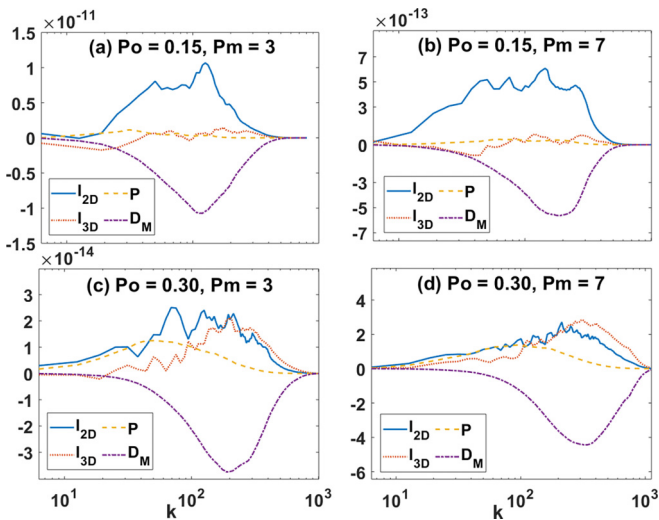

FIG. 5. Shell-averaged spectra of the dynamical terms in spectral magnetic energy given by Eq. (12): energy injection from the background shear flow, P, resistive dissipation D_M, and the contributions from 2D vortices, I_{2D}, and 3D inertial waves, I_{3D}, in the middle of the kinematic stage at (a) Po = 0.15, Pm = 3; (b) Po = 0.15, Pm = 7; (c) Po = 0.3, Pm = 3; and (d) Po = 0.3, Pm = 7.

(i) *The vortical modes* vary only in the horizontal (x, y) plane and are uniform (aligned) along the vertical z axis, having the form of a columnar vortex. In the linear regime, in the absence of precession, these modes are strictly stationary with zero frequency, $\omega = 0$, and in geostrophic balance. However, in the presence of precession, they oscillate in time with a small amplitude around the stationary solution due to the periodic variation of the background flow U_0 [and hence $k_z(t)$]. The velocity of the vortical modes, denoted as u_{2D}, typically has a dominant horizontal component over the vertical one, $u_h = (u_x^2 + u_y^2)^{1/2} \gg u_z$. This *slow* manifold is also referred to as the 2D and three-component (2D-3C) field in the literature, since it varies only in x and y perpendicular to the rotation z axis, but still involves all three components of velocity. Accordingly, the Fourier transform of the vortical modes' velocity, $\bar{u}_{2D}(k_x, k_y, t)$, is, in fact, a function of only k_x, k_y, and time t with zero time-averaged vertical wave number, i.e., $\langle k_z(t) \rangle = k_{z0} = 0$.

(ii) *The inertial wave modes* vary both in the horizontal (x, y) plane and along the z axis. In the linear regime, they oscillate in time with nonzero frequencies $\omega = 2\Omega k_z/k$ and are therefore considered to form the *fast* manifold. In the presence of precession, inertial waves are driven by the precessional instability [35,36] and grow, extracting energy from the background flow U_0. The velocity of these modes, denoted as u_{3D}, has, in general, comparable horizontal and vertical components, $u_h \sim u_z$, while its Fourier transform $\bar{u}_{3D}$ has nonzero average, $\langle k_z(t) \rangle = k_{z0} \neq 0$.

In the turbulent state, the dynamics of vortices and waves become coupled due to strong nonlinearity, which ensures energy transfers between these two modes with different wave numbers and hence variation of their amplitudes with time. As a result, the timescales of the modes change, forming approximately continuous spectra in frequency. A detailed analysis of the energy spectra and nonlinear dynamics of the vortical and inertial wave modes as well as energy transfers between them in physical and Fourier space in precession-driven turbulence was performed in [32,34]. It was shown that for a given Re, at

sufficiently low Po, the dominant modes in the turbulent state are the vortical ones, as most of the turbulent energy resides in these modes. On the other hand, inertial waves become dynamically more important at higher Po, with their energy increasing relative to that of vortices, due to the stronger precessional instability driving these waves. We will show below that the vortical and wave modes play a central role in driving the precession dynamo and determining its spectral dynamics. In particular, the transition in the dynamo behavior with increasing Po is brought about by the changes in the hydrodynamical precession-driven turbulence regimes.

B. Driving mechanisms of the precession dynamo

To understand the roles of the background flow as well as the vortices and inertial wave modes in driving the precession dynamo, we first obtain the equation for the magnetic energy spectrum $\mathcal{E}_M$ by substituting Fourier transform (10) into Eq. (2) and multiplying both sides by the complex conjugate $\bar{\boldsymbol{B}}^*$. Then, in the electromotive force (EMF) $\nabla \times (\boldsymbol{u} \times \boldsymbol{B})$, the velocity is divided into vortical $\boldsymbol{u}_{2D}$ and wave $\boldsymbol{u}_{3D}$ parts, $\boldsymbol{u} = \boldsymbol{u}_{2D} + \boldsymbol{u}_{3D}$, giving

$$\frac{d\mathcal{E}_M}{dt} = P + D_M + I_{2D} + I_{3D}, \tag{12}$$

where $P = \Omega(\bar{\boldsymbol{B}}^*\bar{B}_z + \bar{\boldsymbol{B}}\bar{B}_z^*) \cdot [\boldsymbol{\varepsilon}(t) \times \boldsymbol{e}_z]$ describes energy exchange between the magnetic field and the background flow due to shear, when $P > 0$ energy is injected from the flow into the field. The second term $D_M = -2k^2\mathcal{E}_M/(\text{Re} \cdot \text{Pm}) < 0$ is always negative and describes resistive dissipation. The third I_{2D} and fourth I_{3D} terms describe magnetic energy production, respectively, by vortical and inertial wave modes and are given by $I_{2D} = \text{i}[\bar{\boldsymbol{B}}^* \cdot \boldsymbol{k} \times (\boldsymbol{u}_{2D} \times \boldsymbol{B})_{\boldsymbol{k}} - \bar{\boldsymbol{B}} \cdot \boldsymbol{k} \times (\boldsymbol{u}_{2D} \times \boldsymbol{B})_{\boldsymbol{k}}^*]/2$ and $I_{3D} = \text{i}[\bar{\boldsymbol{B}}^* \cdot \boldsymbol{k} \times (\boldsymbol{u}_{3D} \times \boldsymbol{B})_{\boldsymbol{k}} - \bar{\boldsymbol{B}} \cdot \boldsymbol{k} \times (\boldsymbol{u}_{3D} \times \boldsymbol{B})_{\boldsymbol{k}}^*]/2$, where the subscript $\boldsymbol{k}$ denotes the Fourier transforms of the EMF contributions coming from the velocity fields $\boldsymbol{u}_{2D}$ and $\boldsymbol{u}_{3D}$ associated with these two subsets of modes.

Figure 5 shows the shell-averaged spectra of these four terms $P(k)$, $D_M(k)$, $I_{2D}(k)$, $I_{3D}(k)$ in the middle of the kinematic stage. Depending on Po and Pm, either only vortices or jointly vortices, waves, and the background shear are responsible for the magnetic field amplification. At smaller Po = 0.15, I_{2D} is positive and much larger than I_{3D} and P, i.e., $I_{2D} \gg P, I_{3D}$, implying that vortices predominantly drive the dynamo, whereas the driving by shear and inertial waves is relatively small [Figs. 5(a) and 5(b)]. As seen from this figure, this process is most efficient at intermediate $10 \lesssim k \lesssim 200$, where I_{2D} is appreciable. As Pm increases, I_{2D} extends a bit to higher k, although its dependence on Pm is weak at this Po, consistent with the behavior of the magnetic energy spectra in Fig. 4(a). It also follows from this trend that the total (over all k) driving by vortices is larger than that of inertial waves, $\int I_{2D}dk/ \int I_{3D}dk = 7.78$ and 10.45 at Pm=3 and 7, respectively.

The dynamics changes qualitatively at higher Po = 0.3—the contribution of inertial waves and the shear in driving the dynamo becomes more appreciable relative to vortices since the corresponding terms I_{3D} and P are now comparable to I_{2D}, as seen in Figs. 5(c) and 5(d) for the same Pm, but they operate at different wave numbers. Specifically, the waves amplify the

magnetic field at higher $k \gtrsim 100$, while the shear operates at intermediate wave numbers, $10 \lesssim k \lesssim 200$. With increasing Pm, I_{3D} dominates more over I_{2D} and P at large k, with its peak also shifting to higher k. So, at larger Pm, the 3D waves become the main driver of the dynamo at small scales, while the vortices and the shear dominate at lower and intermediate k [Fig. 5(d)]. Accordingly, in this regime, the total driving by vortices and waves is comparable, $\int I_{2D}dk/ \int I_{3D}dk = 1.06$ and 0.73 at Pm=3 and 7, respectively, although the second value is smaller due to the increased role of waves with increasing Pm.

Thus, Fig. 5 clearly shows a remarkable transition in the precession dynamo dynamics from a predominantly vortex-driven regime at lower Po = 0.15 to a more complex regime driven jointly by vortices, waves, and shear at higher Po = 0.3. This is actually related to the transition in the precession-driven turbulence regimes, as noted in Sec. IV A, from the vortex-dominated state at lower Po to the state at higher Po where vortices and waves coexist and nonlinearly transfer energies between each other and the background flow.

V. CONCLUSIONS

In this paper, we have revealed and analyzed magnetic dynamo action powered by precession-driven *turbulence*, which is capable of exponentially amplifying the magnetic field. We showed that during the kinematic stage, the growth rate of the dynamo increases with the Poincaré (Po) and the magnetic Prandtl (Pm) numbers for the considered ranges of these two parameters. The critical Po_c for the dynamo onset decreases with increasing Pm, that is, the dynamo sets in at lower Po the higher Pm is.

Although our model is local, it captures two basic ingredients of precessional turbulence: 2D vortices and 3D inertial waves. Thus, this model is able to cover a broader range of length scales than global ones—from the system size, through intermediate scales mainly occupied by vortices, down to the shortest dissipation scales mainly occupied by inertial waves in our model. Previous works on the precession dynamo in global settings [15,16,18,19,21,26–30] emphasized the significance of large-scale vortices as a primary driver for large-scale magnetic field amplification, suggesting that the nature of the dynamo is closely linked to this flow pattern. This work, going beyond those findings, has demonstrated the strong influence of the precession on the dynamo properties over a broad range of scales, thereby providing deeper insights into the dynamo action (growth rate, energy spectra, driving mechanism) over these scales. To achieve this, we have performed spectral analysis of the dynamics in Fourier space, quantifying the growth rate of the magnetic energy spectrum and the contributions from vortices, base flow shear, and waves in driving the dynamo as a function of wave number. The main result of such a spectral analysis is a notable transition in the precession dynamo dynamics from a predominantly vortex-driven regime at smaller Po $\lesssim 0.15$ to a more complex regime at larger Po $\gtrsim 0.15$, where vortices, inertial waves, and background shear act in cooperation to amplify the magnetic field at different scales. Vortices and shear drive the dynamo mostly at large (system-size) scales and especially at intermediate scales, being therefore less sensitive to Pm,

while waves operate mainly at smaller scales, hence they depend more strongly on Pm. This dynamo transition is closely related to the intrinsic changes in the precession-driven turbulence regimes from the vortex-dominated one at smaller Po to one at higher Po where vortices and inertial waves coexist, exchanging energy due to nonlinear transfers [32,34].

The sequence of processes leading to the dynamo action in the present problem (a precessional flow subject to instability → turbulence → vortices → dynamo) resembles that taking place in rotating convection. As shown in [43], thermal convection in the presence of rotation leads to turbulence and the formation of large-scale vortices, which in turn amplify the magnetic field as a result of induction (stretching) by vortical structures. Thus, these two different (convection and precession) processes share a common generic mechanism—*vortex-induced dynamo*—which we have analyzed in this paper. Thus, this study can be important not only for understanding the magnetic dynamo action in precession-driven flows, but also in a general context of flow systems where vortices emerge and govern the flow dynamics and evolution.

Our results can offer only qualitative insights regarding precession dynamo experiments due to differences in the regimes that are investigated and the setups that are employed. Notably, in the present study, the magnetic Reynolds number $Rm = Pm \cdot Re$, which controls dynamo onset and dynamics in those experiments, takes values $Rm = 3 \times 10^3 – 3 \times 10^5$ corresponding to the considered range of $Pm = 0.1–10$ and $Re = 3 \times 10^4$, that far exceed the current capabilities of experimental facilities (e.g., DRESDYN dynamo experiment [44,45]). Additionally, in experiments, one has to deal with real boundaries of the flow domain, which are excluded in our periodic box. The presence of boundary layers, as highlighted by Gans [46], can be advantageous in experiments by lowering the Rm threshold of the precession dynamo and thus making it easier to excite due to shear in these layers, which, stretching magnetic field lines, expedites the amplification of the field. What we can take away from this study as a guiding principle for future dynamo experiments with precessional driving is that the developed turbulence within the bulk flow itself is conducive to dynamo action. So, an ideal experimental device should reach a high enough precession parameter Po to sustain both the vortices and inertial waves contained in this turbulence, which, as we showed, are capable of efficiently amplifying the magnetic field over a broad range of scales.

Finally, we note that in the present paper, our main goal has been to uncover the dynamo action due to precession-driven turbulence and find conditions under which it exists. However, the ranges of Po, Pm, and Re considered here differ from those in precessing stars and planets. Still, our results can contribute to a better understanding of natural dynamos due to precession. The first step towards extrapolating the present analysis to relevant parameter regimes would be to investigate the effect of increasing Re (which is huge in real astrophysical and geophysical objects, e.g., larger than 10^{10} in stellar interiors [47]) on the dynamo threshold, growth rate, and driving mechanisms in the (Po, Pm) plane. This will allow us to see whether the precession dynamo can extend to even smaller Po and Pm (and larger Re) typical of weakly precessing stars and planets than those considered in this work.

[1] P. H. Roberts, *Lectures on Solar and Planetary Dynamos*, edited by M. R. E. Proctor and A. D. Gilbert (Cambridge University Press, Cambridge, 1995), p. 1.

[2] K. Moffatt and E. Dormy, *Self-Exciting Fluid Dynamos*, Cambridge Texts in Applied Mathematics (Cambridge University Press, Cambridge, 2019).

[3] F. Rincon, Dynamo theories, J. Plasma Phys. **85**, 205850401 (2019).

[4] W. V. R. Malkus, Precession of the earth as the cause of geomagnetism, Science **160**, 259 (1968).

[5] J. Vanyo, A geodynamo powered by luni-solar precession, Geophy. Astro. Fluid. **59**, 209 (1991).

[6] M. Landeau, A. Fournier, H.-C. Nataf, D. Cébron, and N. Schaeffer, Sustaining Earth's magnetic dynamo, Nat. Rev. Earth Environ. **3**, 255 (2022).

[7] R. Lagrange, P. Meunier, F. Nadal, and C. Eloy, Precessional instability of a fluid cylinder, J. Fluid Mech. **666**, 104 (2011).

[8] D. E. Loper, Torque balance and energy budget for the precessionally driven dynamo, Phys. Earth Planet. Inter. **11**, 43 (1975).

[9] M. Rochester, J. Jacobs, D. Smylie, and K. Chong, Can precession power the geomagnetic dynamo? Geophys. J. Intl. **43**, 661 (1975).

[10] A. Giesecke, T. Albrecht, T. Gundrum, J. Herault, and F. Stefani, Triadic resonances in nonlinear simulations of a fluid flow in a precessing cylinder, New J. Phys. **17**, 113044 (2015).

[11] J. Noir, D. Brito, K. Aldridge, and P. Cardin, Experimental evidence of inertial waves in a precessing spheroidal cavity, Geophys. Res. Lett. **28**, 3785 (2001).

[12] P. Meunier, C. Eloy, R. Lafrange, and F. Nadal, A rotating fluid cylinder subject to weak precession, J. Fluid Mech. **599**, 405 (2008).

[13] S. Goto, A. Matsunaga, M. Fujiwara, M. Nishioka, S. Kida, M. Yamato, and S. Tsuda, Turbulence driven by precession in spherical and slightly elongated spheroidal cavities, Phys. Fluids **26**, 055107 (2014).

[14] J. Herault, A. Giesecke, T. Gundrum, and F. Stefani, Instability of precession driven kelvin modes: Evidence of a detuning effect, Phys. Rev. Fluids **4**, 033901 (2019).

[15] V. Kumar, F. Pizzi, A. Giesecke, J. Šimkanin, T. Gundrum, M. Ratajczak, and F. Stefani, The effect of nutation angle on the flow inside a precessing cylinder and its dynamo action, Phys. Fluids **35**, 014114 (2023).

[16] D. Kong, Z. Cui, X. Liao, and K. Zhang, On the transition from the laminar to disordered flow in a precessing spherical-like cylinder, Geophys. Astrophys. Dluid Dyn. **109**, 62 (2015).

[17] F. Marques and J. M. Lopez, Precession of a rapidly rotating cylinder flow: Traverse through resonance, J. Fluid Mech. **782**, 63 (2015).

[18] Y. Lin, P. Marti, J. Noir, and A. Jackson, Precession-driven dynamos in a full sphere and the role of large scale cyclonic vortices, Phys. Fluids **28**, 066601 (2016).

[19] A. Giesecke, T. Vogt, T. Gundrum, and F. Stefani, Nonlinear large scale flow in a precessing cylinder and its ability to drive dynamo action, Phys. Rev. Lett. **120**, 024502 (2018).

[20] T. Albrecht, H. M. Blackburn, J. M. Lopez, R. Manasseh, and P. Meunier, On triadic resonance as an instability mechanism in precessing cylinder flow, J. Fluid Mech. **841**, R3 (2018).

[21] D Cébron, R. Laguerre, J. Noir, and N. Schaeffer, Precessing spherical shells: Flows, dissipation, dynamo and the lunar core, Geophys. J. Intl. **219**, S34 (2019).

[22] J. M. Lopez and F. Marques, Rapidly rotating precessing cylinder flows: Forced triadic resonances, J. Fluid Mech. **839**, 239 (2018).

[23] K. Wu, B. D. Welfert, and J. M. Lopez, Precessing cube: Resonant excitation of modes and triadic resonance, J. Fluid Mech. **887**, A6 (2020).

[24] F. Pizzi, A. Giesecke, and F. Stefani, Ekman boundary layers in a fluid filled precessing cylinder, AIP Adv. **11**, 035023 (2021).

[25] F. Pizzi, A. Giesecke, J. Šimkanin, and F. Stefani, Prograde and retrograde precession of a fluid-filled cylinder, New J. Phys. **23**, 123016 (2021).

[26] A. Tilgner, Precession driven dynamos, Phys. Fluids **17**, 034104 (2005).

[27] C.-C. Wu and P. Roberts, On a dynamo driven by topographic precession, Geophys. Astrophys. Fluid Dyn. **103**, 467 (2009).

[28] L. Cappanera, J.-L. Guermond, J. Léorat, and C. Nore, Two spinning ways for precession dynamo, Phys. Rev. E **93**, 043113 (2016).

[29] O. Goepfert and A. Tilgner, Dynamos in precessing cubes, New J. Phys. **18**, 103019 (2016).

[30] O. Goepfert and A. Tilgner, Mechanisms for magnetic field generation in precessing cubes, Geophys. Astrophys. Fluid Dyn. **113**, 222 (2019).

[31] R. M. Mason and R. R. Kerswell, Chaotic dynamics in a strained rotating flow: A precessing plane fluid layer, J. Fluid Mech. **471**, 71 (2002).

[32] A. J. Barker, On turbulence driven by axial precession and tidal evolution of the spin-orbit angle of close-in giant planets, Mon. Not. R. Astron. Soc. **460**, 2339 (2016).

[33] A. Khlifi, A. Salhi, S. Nasraoui, F. Godeferd, and C. Cambon, Spectral energy scaling in precessing turbulence, Phys. Rev. E **98**, 011102(R) (2018).

[34] F. Pizzi, G. Mamatsashvili, A. Barker, A. Giesecke, and F. Stefani, Interplay between geostrophic vortices and inertial waves in precession-driven turbulence, Phys. Fluids **34**, 125135 (2022).

[35] R. R. Kerswell, The instability of precessing flow, Geophy. Astro. Fluid. **72**, 107 (1993).

[36] R. R. Kerswell, Elliptical instability, Annu. Rev. Fluid Mech. **34**, 83 (2002).

[37] A. Salhi, T. Lehner, and C. Cambon, Magnetohydrodynamic instabilities in rotating and precessing sheared flows: An asymptotic analysis, Phys. Rev. E **82**, 016315 (2010).

[38] J. F. Hawley, C. F. Gammie, and S. A. Balbus, Local Three-dimensional magnetohydrodynamic simulations of accretion disks, J. **440**, 742 (1995).

[39] G. Lesur and P. Y. Longaretti, On the relevance of subcritical hydrodynamic turbulence to accretion disk transport, Astron. Astrophys. **444**, 25 (2005).

[40] A. Alexakis and L. Biferale, Cascades and transitions in turbulent flows, Phys. Rep. **767-769**, 1 (2018).

[41] L. M. Smith and F. Waleffe, Transfer of energy to two-dimensional large scales in forced, rotating three-dimensional turbulence, Phys. Fluids **11**, 1608 (1999).

[42] M. Buzzicotti, H. Aluie, L. Biferale, and M. Linkmann, Energy transfer in turbulence under rotation, Phys. Rev. Fluids **3**, 034802 (2018).

[43] C. Guervilly, D. W. Hughes, and C. A. Jones, Generation of magnetic fields by large-scale vortices in rotating convection, Phys. Rev. E **91**, 041001(R) (2015).

[44] F. Pizzi, A. Giesecke, J. Šimkanin, K. Vivaswat, G. Thomas, and F. Stefani, Numerical and theoretical framework for the DRES-DYN precession dynamo experiment, Magnetohydrodynamics **58**, 445 (2022).

[45] F. Stefani, T. Albrecht, G. Gerbeth, A. Giesecke, T. Gundrum, J. Herault, C. Nore, and C. Steglich, Towards a precession driven dynamo experiment, Magnetohydrodynamics **51**, 275 (2015).

[46] R. F. Gans, On hydromagnetic precession in a cylinder, J. Fluid Mech. **45**, 111 (1971).

[47] M. Viallet, C. Meakin, D. Arnett, and M. Mocák, Turbulent convection in stellar interiors. III: Mean-field analysis and stratification effects, Astrophys. J. **769**, 1 (2013).